Check for updates

AGU ADVANCING EARTH AND SPACE SCIENCES

Geophysical Research Letters

RESEARCH LETTER
10.1029/2025GL119484

Persisting Modulation of Interdecadal Pacific Oscillation on Near-Future Winter Precipitation Projections in Northern Europe

Mengyuan Yao[1,2], **Haosu Tang**[3], **and Gang Huang**[1,2]

[1]State Key Laboratory of Earth System Numerical Modeling and Application, Institute of Atmospheric Physics, Chinese Academy of Sciences, Beijing, China, [2]University of Chinese Academy of Sciences, Beijing, China, [3]School of Geography and Planning, University of Sheffield, Sheffield, UK

Abstract European winter precipitation profoundly influences regional hydroclimate, yet the relative roles of internal variability and external forcing in its decadal changes remain elusive. Using large-ensemble climate simulations, we identify the Interdecadal Pacific Oscillation (IPO) as a potential driver of interdecadal changes in winter northern European precipitation. During the 1980–2014 IPO phase transition, internal variability induced a drying trend of −0.07 mm day^{-1} (35 years)$^{-1}$, offsetting a concurrent externally forced wetting trend of +0.19 mm day^{-1} (35 years)$^{-1}$. This influence arises from IPO-related modulation of atmospheric circulation and moisture transport. The persistence of IPO–WNEP linkages into 2015–2050 suggests that internal variability may continue to shape near-future hydroclimate. Accounting for IPO-related influences reduces projection uncertainty by 30% historically and 20% in the near future. These results highlight the critical role of internal variability in long-term European precipitation trends and emphasize its relevance for regional water resource planning.

Plain Language Summary Winter precipitation in Europe is highly variable from decade to decade, with important consequences for water resources, agriculture, and ecosystems. Understanding the drivers of these changes is crucial for improving climate projections and managing regional risks. In this study, we use climate model large ensembles to separate the effects of external human-induced climate change from internal natural variability. We find that a large share of the decadal fluctuations in northern European winter precipitation is linked to the Interdecadal Pacific Oscillation (IPO), a long-term mode of climate variability in the Pacific Ocean. During its transition from a positive to a negative phase (1980–2014), the IPO triggered a drying trend in Europe by altering large-scale atmospheric circulation and reducing moisture transport into the region. This drying trend nearly canceled out the wetting effect expected from human-induced greenhouse gas forcing over the same period. Looking ahead, the IPO is projected to continue influencing precipitation in the coming decades (2015–2050). Importantly, accounting for IPO-related variability reduces uncertainty in precipitation projections by up to 30%. These results emphasize that natural variability should be considered alongside human-induced change to better anticipate Europe's future hydroclimate.

Key Points:

- Interdecadal Pacific Oscillation (IPO) drove European winter drying during 1980–2014, offsetting externally forced wetting
- The IPO influences European winter precipitation via atmospheric teleconnections that modulate moisture transport
- Accounting for IPO-related variability reduces precipitation projection uncertainty by 20%–30% for both historical and near-future periods

Supporting Information:

Supporting Information may be found in the online version of this article.

Correspondence to:

H. Tang and G. Huang,
haosu.tang@sheffield.ac.uk;
hg@mail.iap.ac.cn

Citation:

Yao, M., Tang, H., & Huang, G. (2026). Persisting modulation of Interdecadal Pacific Oscillation on near-future winter precipitation projections in northern Europe. *Geophysical Research Letters*, *53*, e2025GL119484. https://doi.org/10.1029/2025GL119484

Received 16 SEP 2025
Accepted 23 JAN 2026

Author Contributions:

Conceptualization: Mengyuan Yao, Haosu Tang
Data curation: Mengyuan Yao
Formal analysis: Mengyuan Yao, Haosu Tang
Funding acquisition: Gang Huang
Investigation: Mengyuan Yao
Methodology: Mengyuan Yao, Haosu Tang
Project administration: Gang Huang
Resources: Mengyuan Yao
Software: Mengyuan Yao
Supervision: Haosu Tang, Gang Huang
Validation: Mengyuan Yao
Visualization: Mengyuan Yao

© 2026 The Author(s).
This is an open access article under the terms of the Creative Commons Attribution-NonCommercial License, which permits use, distribution and reproduction in any medium, provided the original work is properly cited and is not used for commercial purposes.

1. Introduction

In recent decades, large parts of Europe have experienced increasingly prolonged and widespread droughts (van der Woude et al., 2023), imposing annual losses of approximately 9 billion euros across the European Union and the United Kingdom and disrupting agriculture, energy, water supply, and transportation (Cammalleri et al., 2020; Garrido-Perez et al., 2024; Toreti et al., 2022). Notably, record-breaking droughts in Europe, including those of 2015, 2016/17 and 2018, are closely linked to deficient winter/spring precipitation followed by extreme summer heatwaves (García-Herrera et al., 2019; Laaha et al., 2017; Rakovec et al., 2022). Rising temperatures and increased potential evapotranspiration have further amplified drought risk, especially in central and southern Europe (Ionita & Nagavciuc, 2021; Vicente-Serrano et al., 2014). Long-term observations reveal a significant drying trend in the Mediterranean and parts of Russia, while northern Europe has experienced a pronounced wetting trend (Bordi et al., 2009; Caloiero et al., 2018; Hoerling et al., 2012). This meridional "see-saw" pattern of drying in the south and wetting in the north has persisted for centuries and is projected to persist (An et al., 2023; Spinoni et al., 2018; Trnka et al., 2016). Accurate simulation and projection of precipitation in

Writing – original draft: Mengyuan Yao
Writing – review & editing: Mengyuan Yao, Haosu Tang, Gang Huang

these climate-sensitive regions are thus crucial for managing agriculture, water resources, energy systems, and overall societal resilience.

On the interannual timescale, the meridional precipitation contrast is linked to sea surface temperature (SST) variability and large-scale atmospheric circulation, particularly El Niño–Southern Oscillation (ENSO) and North Atlantic Oscillation (NAO), which together account for about one-fifth of European precipitation variability (Fereday et al., 2018; Herweijer & Seager, 2008; McKenna & Maycock, 2022). Meanwhile, ENSO–NAO linkages coupled with volcanic eruption could also exert pronounced influences on high-latitude climate (Dogar et al., 2023, 2025). In addition, interactions among basins can potentially amplify European winter climate anomalies, particularly when SST signals are in phase (Gouirand & Moron, 2003; Mathieu et al., 2004; Scaife et al., 2014). While some analyses claim that ENSO events may have limited influence on European precipitation, such discrepancies likely stem from nonlinear dynamics (Brönnimann, 2007; Mathieu et al., 2004), low signal-to-noise ratios in projecting individual ENSO events (Molteni & Brookshaw, 2023), and interference from Atlantic variability (Mathieu et al., 2004).

On decadal timescales, Pacific Decadal Oscillation (PDO) plays a major role in modulating European precipitation patterns. Negative PDO phase typically brings drier conditions to southern Europe and wetter conditions to Scandinavian Peninsula. These impacts arise partly through modulation of ENSO characteristics (Verdon & Franks, 2006) and stratospheric responses mediated by Pacific–North America-like teleconnections (Rao et al., 2019; Yu & Zwiers, 2007). Additionally, moisture variability in mid-latitude Europe is also influenced by multidecadal variability over the Atlantic basin, namely Atlantic Multidecadal Variability (AMV) (Ionita et al., 2021). On the other hand, externally forced changes, especially those induced by greenhouse gas emissions, have been shown to favor the meridional "see-saw" pattern in winter European precipitation (Christidis & Stott, 2022). However, the net effect of greenhouse gas forcing may be partially offset by opposing influence of anthropogenic aerosols (Christidis & Stott, 2022). As European aerosol emissions continue to decline, their influences combined with those of increasing greenhouse gases are expected to intensify in the coming decades (Samset et al., 2018).Winter meteorological droughts and floods are projected to exert increasingly severe impacts across Europe under continued climate change. However, the relative contributions of external forcing and internal variability to interdecadal changes in European precipitation remain elusive, particularly over northern Europe, where a pronounced wetting trend emerges within the European precipitation see-saw (Hoerling et al., 2012). Recent advances suggest that leveraging dominant climate modes may offer a promising approach for constraining inter-member variability and thereby reducing uncertainties in near-future projections. In this study, we analyze interdecadal changes in winter northern European precipitation (WNEP) over 45–60°N latitude band using large ensemble climate simulations to quantify the respective roles of internal variability and external forcing, excluding southern Europe where anthropogenically forced responses are controversial and undetectable (Peña-Angulo et al., 2020; Vicente-Serrano et al., 2025). Our findings aim to inform strategies for narrowing near-term projection uncertainties and improving the robustness of regional climate predictions in northern Europe.

2. Materials and Methods

2.1. Data

Observational monthly precipitation and SST used in this study are obtained from the Climatic Research Unit (CRU) high-resolution gridded data set (version 4.07) (Harris et al., 2020) and Extended Reconstructed SST (ERSST) version 5 (Huang et al., 2017), respectively. We incorporate another two data sets separately for verification: Global Precipitation Climatology Center (GPCC) monthly product (version 2022) (Schneider et al., 2022) and University of Delaware (UDel) Air Temperature & Precipitation data set (version v4.01) (Matsuura & Willmott, 2015) for precipitation, and Hadley Center Sea Ice and SST data set (HadISST) (Rayner et al., 2003) and Kaplan Extended SST V2 (Kaplan et al., 1998) data sets for SST. Detailed information of these data sets is provided in Table S1 in Supporting Information S1.

We employ two sets of large-ensemble climate model outputs, each comprising 50 members for historical simulations (1850–2014) and future projections (2015–2100) based on the Shared Socioeconomic Pathway 5–8.5 scenario. These ensembles could serve as powerful tools to disentangle the roles of internal climate variability and external forcing (Deser et al., 2020; Huang, Zhou, Turner, et al., 2020). The first model, Canadian Earth System Model version 5 (CanESM5) (Swart et al., 2019), is used to distinguish the relative contributions of external

19448007, 2026, 3, Downloaded from https://agupubs.onlinelibrary.wiley.com/doi/10.1029/2025GL119484 by Gang Huang - Institution Of Atmospheric Physics , Wiley Online Library on [02/02/2026]. See the Terms and Conditions (https://onlinelibrary.wiley.com/terms-and-conditions) on Wiley Online Library for rules of use; OA articles are governed by the applicable Creative Commons License

19448007, 2026, 3, Downloaded from https://agupubs.onlinelibrary.wiley.com/doi/10.1029/2025GL119484 by Gang Huang - Institution Of Atmospheric Physics , Wiley Online Library on [02/02/2026]. See the Terms and Conditions (https://onlinelibrary.wiley.com/terms-and-conditions) on Wiley Online Library for rules of use; OA articles are governed by the applicable Creative Commons License

forcing and internal climate variability. The second model, Model for Interdisciplinary Research on Climate version 6 (MIROC6) (Tatebe et al., 2019), serves to verify the conclusions. Additionally, the pre-industrial control (piControl) simulation, which spans 2,000 years under fixed greenhouse gas concentrations and forcing levels as in 1850, is used as well.

All the observations and model simulations are bilinearly interpolated to a uniform 1×1 horizontal grid before analysis. An 11-year running average is applied to the raw data to remove interannual signals and extract interdecadal variability. Boreal winter months are defined as December (of the previous year), January, and February. The periods 1980–2014 and 2015–2050 are considered as the historical and near-term future periods, respectively, with anomalies calculated relative to the 1951–2000 average. The results of this study are robust against different choices of climate norms. Additionally, statistical procedures are detailed in Text S1 in Supporting Information S1.

2.2. Adjusting WNEP Uncertainty by Climate Mode

To identify the contributions of climate modes to interdecadal WNEP changes, the following linear regression is performed to separate the influence of climate mode in each ensemble member:

$$P(i,t) = s(i) \cdot \mathrm{Index}(i,t) + P_{\mathrm{non\text{–}Index}}(i), i = 1,2,\ldots,50 \quad (1)$$

where $P(i,t)$ denotes WNEP in the i-th ensemble member at time t. The regression coefficient $s(i)$ indicates the magnitude of WNEP changes with normalized $\mathrm{Index}(i,t)$ changes, such as Interdecadal Pacific Oscillation (IPO), and $P_{\mathrm{non-Index}}(i)$ represents the WNEP response to external forcing and other internal variability without the effects of climate indices.

In large-ensemble simulations, all members are driven by identical external forcing, while inter-member or internal variability in simulated WNEP trends primarily arises from differing realizations and phase evolutions of climate modes (Hawkins & Sutton, 2011). If a strong inter-member relationship exists between trends of a given climate mode and WNEP, constraining the mode-related trends of $s(i) \cdot \frac{\partial \mathrm{Index}(i,t)}{\partial t}$ can effectively reduce inter-member uncertainty of WNEP trends, which are estimated as:

$$\frac{\partial P_{\mathrm{adj}}(i,t)}{\partial t} = s(i) \cdot \frac{\partial \mathrm{Index}(i,t)}{\partial t} + \frac{\partial P_{\mathrm{non\text{–}Index}}(i,t)}{\partial t}, i = 1,2,\ldots,50 \quad (2)$$

where $\frac{\partial P_{\mathrm{adj}}(i)}{\partial t}$ represents the adjusted WNEP trends and varies across ensemble members. s, Index, and $P_{\mathrm{non-Index}}$ are the same as in Equation 1. $s(i) \cdot \frac{\partial \mathrm{Index}(i,t)}{\partial t}$ denotes the climate mode-contributed WNEP trends during the historical period (1980–2014), matching the complete peak-to-tough phase transition of IPO, or subsequent 35-year period in the near future (2015–2050). For the period 1980–2014, $\frac{\partial \mathrm{Index}(i,t)}{\partial t}$ is set as the observed trends, while for 2015–2050, it is set as a constant value of ± 2, lying within one STD of the normalized climate mode trends across the 50 members and thereby representing a physically plausible realization of inter-member variability. This definition also represents the full phase transition of specific climate modes, minimizing truncation biases associated with incomplete cycles, consistent with the previous study (Huang, Zhou, Dai, et al., 2020). The result of $\frac{\partial P_{\mathrm{adj}}(i)}{\partial t}$ could estimate the potential for the specified climate variability to narrow uncertainties of WNEP trend with a certain phase transition pattern and fixed magnitude, as summarized schematically in Figure S1 in Supporting Information S1.

Additionally, the probabilities of the positive trend (PT), extreme drying trend (EDT), and extreme wetting trend (EWT) indices before and after the WNEP adjustment are also estimated as documented in Text S2 in Supporting Information S1.

3. Results

3.1. Observed and Simulated WNEP Changes

Over northern Europe, a pronounced wetting trend is observed during 1951–2014, with observations showing an increase of 0.05 mm day^{-1} (35-year)$^{-1}$, ranging within 0.02–0.09 mm day^{-1} (35-year)$^{-1}$ across observational

10.1029/2025GL119484

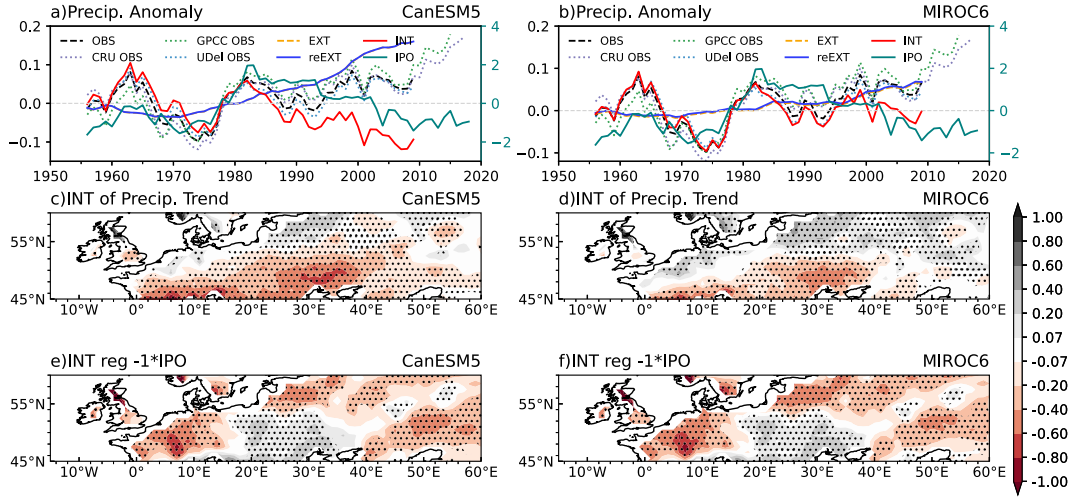

Figure 1. (a, b) Time series of precipitation anomalies (units: mm day^{-1}) in three observational data sets of Climatic Research Unit (blue dotted line), Global Precipitation Climatology Center (purple dotted line), and Udel (green dotted line), along with the normalized IPO index in the observation (teal line). The black dashed line indicates the ensemble mean of observational data sets. The yellow dashed and blue solid lines indicate the original and rescaled externally forced precipitation anomalies, respectively, derived from the CanESM5 and MIROC6 models. The red solid line indicates the internally generated precipitation anomalies. (c, d) Internally driven winter northern European precipitation (WNEP) trends (units: mm day^{-1} (65-year)$^{-1}$) after removing the rescaled MME in CanESM5 and MIROC6 models during 1951–2014, respectively. (e, f) Regression of 11-year running averaged internally driven WNEP (units: mm day^{-1}) onto opposite values of normalized IPO index in CanESM5 and MIROC6 models during 1951–2014, respectively. Dots denote regions with significant regression coefficients at the 90% confidence level.

data sets (Figures 1a and 1b). This trend is largely attributed to external forcing, which accounts for approximately 92% [50%–129%] of the total change, based on the CanESM5 ensemble mean of 0.04 mm day^{-1} (35-year)$^{-1}$ with inter-member trends ranging from −0.04–0.23 mm day^{-1} (35-year)$^{-1}$, indicating substantially larger model uncertainty than suggested by observations. After removing the rescaled externally forced component from observations (Text S4 in Supporting Information S1), internal variability contributes a modest yet non-negligible drying signal of −0.004 mm day^{-1} (35-year)$^{-1}$. These patterns are consistent across large ensemble models of CanESM5 and MIROC6 over extensive areas of northern Europe (Figures 1c and 1d). From 1980 to 2014, the long-term internally driven drying intensifies to −0.11 mm day^{-1} (35-year)$^{-1}$. This period coincides with a sequence of extreme hydroclimatic events, including mega heatwaves and record-breaking droughts (García-Herrera et al., 2019; Ionita & Nagavciuc, 2021; Toreti et al., 2022). The internal drying and its associated variability highlight the importance of understanding the underlying mechanisms, as well as the implications for uncertainty in precipitation projections.

During 1951–2014, both observed WNEP and its internal-driven component exhibit significant correlations with IPO, with coefficients of 0.65 and 0.45 based on effective degrees of freedom of 16 and 21 ($P < 0.05$), respectively. Spatially, internal variability shows a distinct IPO-related pattern: a significant positive correlation over western and eastern Europe, and a negative correlation over central Europe (Figures 1e and 1f). On the interdecadal timescale, the 11-year running averaged WNEP regressed onto IPO index reveals the driest centers over Eastern European Plain. This is generally consistent with the ensemble mean of model simulations, which depicts more homogenous drying across the whole northern Europe (Figures S2a–S2b in Supporting Information S1). Regressed SST similarly reveals the negative IPO-like pattern in both observation and ensemble mean (Figures S2c–S2d in Supporting Information S1). These analyses suggest that WNEP variability may be modulated by IPO. Before quantifying the potential contribution of IPO to WNEP variability, we evaluate the performance of ensemble mean of model simulations, which well reproduces observed WNEP patterns for 1951–2014 (Figures S2e–S2f in Supporting Information S1).

19448007, 2026, 3, Downloaded from https://agupubs.onlinelibrary.wiley.com/doi/10.1029/2025GL119484 by Gang Huang - Institution Of Atmospheric Physics , Wiley Online Library on [02/02/2026]. See the Terms and Conditions (https://onlinelibrary.wiley.com/terms-and-conditions) on Wiley Online Library for rules of use; OA articles are governed by the applicable Creative Commons License

19448007, 2026, 3, Downloaded from https://agupubs.onlinelibrary.wiley.com/doi/10.1029/2025GL119484 by Gang Huang - Institution Of Atmospheric Physics , Wiley Online Library on [02/02/2026]. See the Terms and Conditions (https://onlinelibrary.wiley.com/terms-and-conditions) on Wiley Online Library for rules of use; OA articles are governed by the applicable Creative Commons License

3.2. IPO Modulation of WNEP Changes

Using random 600-year piControl simulations without external forcing, interdecadal WNEP and SST regression against IPO index confirms a robust relationship that decrease in WNEP aligns with the negative phase of IPO-like SST anomaly (Figure S3 in Supporting Information S1). Meanwhile, a significant positive correlation at the decadal timescale with effective degree of freedom of 71 emerges between the 35-year running averaged WNEP and IPO index.

Given the persistent phase transition of the IPO, the period 1980–2014—marking a complete shift from positive to negative phase—is further selected to investigate its modulation on WNEP. Observed SST trends during this period exhibited a robust La Niña-like pattern, characterized by tropical central and eastern Pacific cooling and Indo–western Pacific warming (Figure S4 in Supporting Information S1). Normalization is conducted to eliminate the IPO's amplitude effects, allowing us to examine distinct IPO phase evolutions among the CanESM5 members during the historical period (1980–2014). Observed IPO trends fall within simulated ranges (−4.59 to 4.52 per 35-year), with the observed IPO trend at −4.09 per 35-year (Figures S5–S7 in Supporting Information S1). To isolate IPO's contribution to WNEP variability, we separate IPO-related and IPO-independent WNEP components using linear regressions. Aligning each member's IPO evolution with observed phase shift allows adjusting historical WNEP trends accordingly. The adjustment integrates both hypothetical impact of observed IPO shifts and residual variability from other climate variability and external forcing. Results show that IPO-independent responses contribute 0.13 mm day^{-1} (35-year)$^{-1}$ to the ensemble mean WNEP trend of 0.19 mm day^{-1} (35-year)$^{-1}$ (Figure S5b in Supporting Information S1, tomato and light gray bars). After IPO adjustment, the WNEP trend declines to 0.12 mm day^{-1} (35-year)$^{-1}$, indicating a drying response to IPO of −0.01 mm day^{-1} (35-year)$^{-1}$ compared to original 0.06 mm day^{-1} (35-year)$^{-1}$, aligning more closely with observed 0.05 mm day^{-1} (35-year)$^{-1}$, ranging 0.04–0.06 mm day^{-1} (35-year)$^{-1}$ across CRU, GPCC, and UDel products (Figure 1a). This also suggests that internal component related with observational IPO shifts by −0.07 mm day^{-1} (35-year)$^{-1}$ could substantially offset the wetting trend of 0.19 mm day^{-1} (35-year)$^{-1}$ caused by external forcing. Meanwhile, the uncertainty is constrained by 30%, decreasing from 0.20 to 0.14 mm day^{-1} (35-year)$^{-1}$ after excluding the inter-member spread of IPO phase shifts in each realization, as verified by alignment with observational reference (Figure S5c in Supporting Information S1). Additionally, sensitivity analyses using alternative IPO definitions and running-window lengths consistently confirm the robustness of the IPO influence on adjusted WNEP trends and on the historical uncertainty constraint by the range of 25%–35% (Table S3 in Supporting Information S1). Therefore, IPO phase transitions play a key role in narrowing uncertainty in recent WNEP trends.

3.3. Near-Term Projection of WNEP Constrained by IPO

Beyond reconciling observation–model discrepancies of climate change impacts, constraint framework could be explored in near-term future (2015–2050) due to the strong positive correlation of 0.50 between trends in WNEP and IPO index (Figure S5d in Supporting Information S1). This technique is likely most effective in the near future when inter-member variability dominates uncertainty of European winter precipitation, followed by model uncertainty, whereas scenario uncertainty remains negligible (Deser et al., 2017; Hawkins & Sutton, 2011). The externally forced WNEP changes, as shown in the ensemble mean of the CanESM5 simulations, reveal a slightly homogenous wetting trend (Figure 2a). However, the magnitude of internal variability across model realizations remains comparable to the forced signal, leading to a low signal-to-noise ratio (SNR), calculated as the absolute value of externally forced signal divided by STD of internal variability, ranging from 0.4 to 1.2 across much of northern Europe (Figures 2b and 2c). This implies that inter-member spread may act as the primary barrier to detecting the external forcing signal. Notably, lower SNRs coincide with regions influenced by the subtropical westerly jet, which could be modulated by warmer Pacific SST anomalies, strengthening the westerlies and increasing moisture transport from the North Atlantic into northern Europe (Shaman & Tziperman, 2011). For the near future, projected WNEP trends span from 0.08 to 0.62 mm day^{-1} (35-year)$^{-1}$ (5th–95th percentile), with 100% of realizations exhibiting positive trends (Figure 2e inset Figure). Given the pronounced uncertainty of WNEP changes, two sub-ensemble sets are selected: five driest (Dry5) and five wettest (Wet5) members over northern Europe. The difference reveals widespread drying in the Dry5 relative to Wet5 across most of northern Europe, except around the Alpes—possibly due to its high topography (Figure 2d). Despite an ensemble-mean increase of 0.34 mm day^{-1} (35-year)$^{-1}$ in externally forced WNEP, the Dry5 and Wet5 sub-ensemble means exhibit markedly divergent trends of 0.08 and 0.62 mm day^{-1} (35-year)$^{-1}$, respectively (Figure 2e). This stark

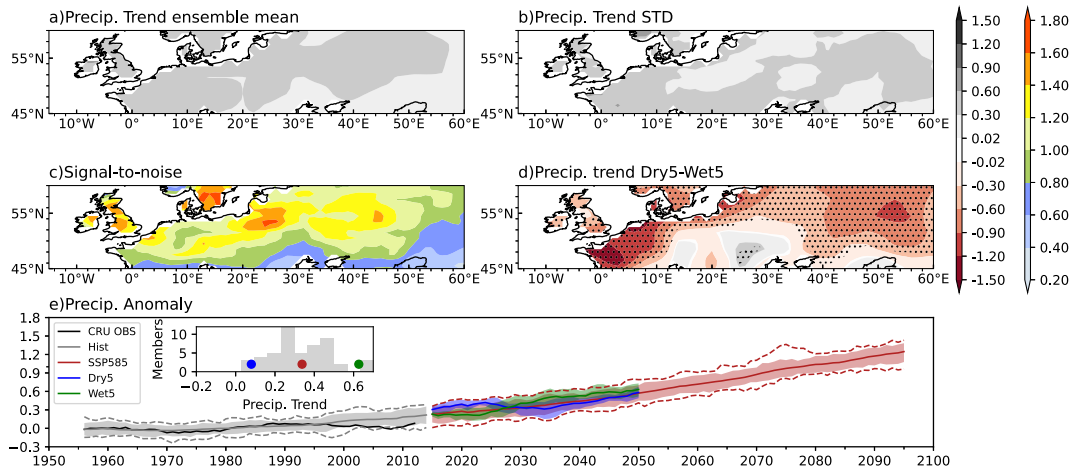

Figure 2. Winter northern European precipitation (WNEP) trends (units: mm day^{-1} (35-year)$^{-1}$) under SSP5–8.5 scenario during 2015–2050 for (a) ensemble mean, (b) inter-member STD, (c) signal-to-noise ratio, and (d) difference in WNEP trends between the 5 driest and 5 wettest members in CanESM5. Dots denote regions with significant differences between the 5 driest and 5 wettest members at the 90% confidence level. (e) Time series of 11-year running averaged WNEP anomalies (units: mm day^{-1}, relative to the 1951–2000 average). Gray and red lines show historical and SSP5–8.5 simulations, respectively, with shading indicating the 5th–95th percentile range, thick solid lines for the ensemble mean, and dashed lines for the maximum and minimum across all 50 members. Blue and green shadings indicate the 5 driest and 5 wettest members under the SSP5–8.5 scenario, respectively. The inset in panel (e) shows the histogram of WNEP trends during 2015–2050. The red, blue, and green dots mark the ensemble mean of 50 members, 5 driest, and 5 wettest members, respectively.

contrast highlights that inter-member variability, rather than external forcing, dominates the spread in near-future projections of WNEP, underscoring the need to constrain internal variability across members for more reliable projections.

To assess robustness, similar analyses are conducted using MIROC6 simulations (Figure S8 in Supporting Information S1). The ensemble means and STD of WNEP trends in MIROC6 resemble those in CanESM5, albeit with weaker external signals and larger inter-member spread (Figures S8a and S8b in Supporting Information S1). As a result, the SNR is significantly smaller in MIROC6, falling below 0.8 in northern Europe (Figure S8c in Supporting Information S1). As expected, differences between the Dry5 and Wet5 members in MIROC6 show a homogeneous significant drying pattern (Figure S8d in Supporting Information S1). The inter-member projection trends are more dispersed in MIROC6, reflected by a wider 5th to 95th percentile range of −0.33 to 0.32 mm day^{-1} (35-year)$^{-1}$, with only 50% of members showing positive trends (Figure S8e in Supporting Information S1). The sub-ensemble averaged trends for Dry5 and Wet5 are −0.30 and 0.28 mm day^{-1} (35-year)$^{-1}$, respectively, indicating a more pronounced contrast and elevated uncertainty in MIROC6 projections.

We further examine the 11-year running averaged SST trends and SST regression onto WNEP based on differences between near-future sub-ensemble outputs. Both exhibit a prominent negative IPO-like pattern, closely resembling observational regressions (Figures 3g and 3h and Figure S2c in Supporting Information S1), confirming that IPO phase shift remains the dominant driver of WNEP trend uncertainty from recent decades into the near future. Dynamical processes, rather than thermodynamic effects, account for 80% of the projected water vapor transport (Figures 3a and 3d). Horizontal moisture divergence plays a major role in drying northern Europe, while the vertical also crucial with anomalous subsidence and increased moisture with height, especially in western Europe (Figures 3a–3d). The dynamically vertical and thermodynamical moisture transport are further decomposed, among which the anomalous horizontal divergence ($-<\bar{q}\nabla\overrightarrow{V'}>$) and vertical advection of background moisture ($-<\omega'\frac{\partial\bar{q}}{\partial p}>$) play dominant roles. Anomalous horizontal divergence hampers moisture convergence and inhibits the precipitation conditions, while subsidence over western Europe dries the air from the upper troposphere to lower levels, suppressing near-surface saturation and precipitation (Figures 3e and 3f). The overweighted divergence- and subsidence-induced drying is linked to high pressure anomalies over much of Europe. This pattern could be induced by pure interdecadal Pacific SST signals after removing interannual Niño 3.4 signal, and forms part of an eastward-propagating Rossby wave train that originates from the North Pacific

19448007, 2026, 3, Downloaded from https://agupubs.onlinelibrary.wiley.com/doi/10.1029/2025GL119484 by Gang Huang - Institution Of Atmospheric Physics , Wiley Online Library on [02/02/2026]. See the Terms and Conditions (https://onlinelibrary.wiley.com/terms-and-conditions) on Wiley Online Library for rules of use; OA articles are governed by the applicable Creative Commons License

10.1029/2025GL119484

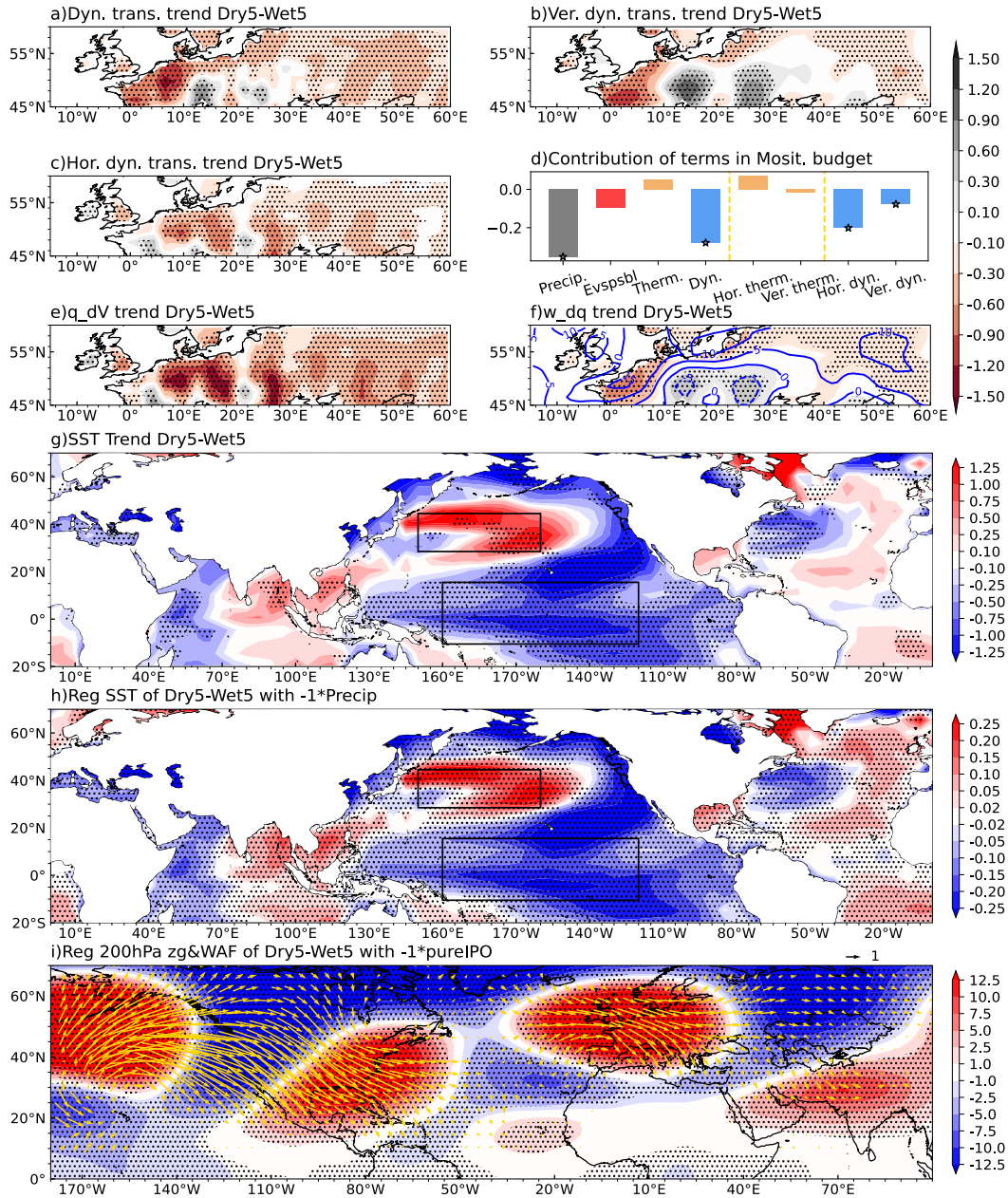

Figure 3. Differences of (a) dynamic water vapor transport, (b) its vertical and (c) horizontal component, and (d) contributions of individual moisture budget terms (units: mm day^{-1} (35-year)$^{-1}$) between the 5 driest and 5 wettest members under the SSP5–8.5 scenario in CanESM5 during 2015–2050. Yellow dashed lines divide the components into three sectors. Stars identify winter northern European precipitation (WNEP) changes and major contributing terms in each sector. In the first sector, bars from left to right indicate precipitation, evaporation, thermodynamic, and dynamic terms. The second and third sectors show the horizontal and vertical decomposition of thermodynamic and dynamic terms, respectively panels (e, f) Same as panel (a), but for $-<\overline{q}\,\nabla\,\overrightarrow{\mathrm{V}'}>$ and $-<\omega'\frac{\partial\overline{q}}{\partial p}>$ (units: mm day^{-1} (35-year)$^{-1}$). The blue contours in panel (f) indicate the vertically integrated vertical velocity (units: 10^3 Pa s^{-1} (35-year)$^{-1}$). (g) sea surface temperature (SST) trend differences (shading; units: K (35-year)$^{-1}$) between the 5 driest and 5 wettest members under the SSP5–8.5 scenario in CanESM5 during 2015–2050. panel (h) Same as panel (g), but for regression of SST (units: K differences onto the 11-year running averaged normalized WNEP. Panels (i) Same as panel (g), but for regression of 200-hPa geopotential height (units: m) differences and the corresponding wave activity flux (vectors; 10^3 units: m^2 s^{-2}) onto the 11-year running averaged normalized pure IPO index after Niño 3.4 signal removed. Dots denote regions with significant differences between the 5 driest and 5 wettest members in panels (a–c, e, and f) and significant regression coefficients in panel (f) at the 90% confidence level.

19448007, 2026, 3, Downloaded from https://agupubs.onlinelibrary.wiley.com/doi/10.1029/2025GL119484 by Gang Huang - Institution Of Atmospheric Physics , Wiley Online Library on [02/02/2026]. See the Terms and Conditions (https://onlinelibrary.wiley.com/terms-and-conditions) on Wiley Online Library for rules of use; OA articles are governed by the applicable Creative Commons License

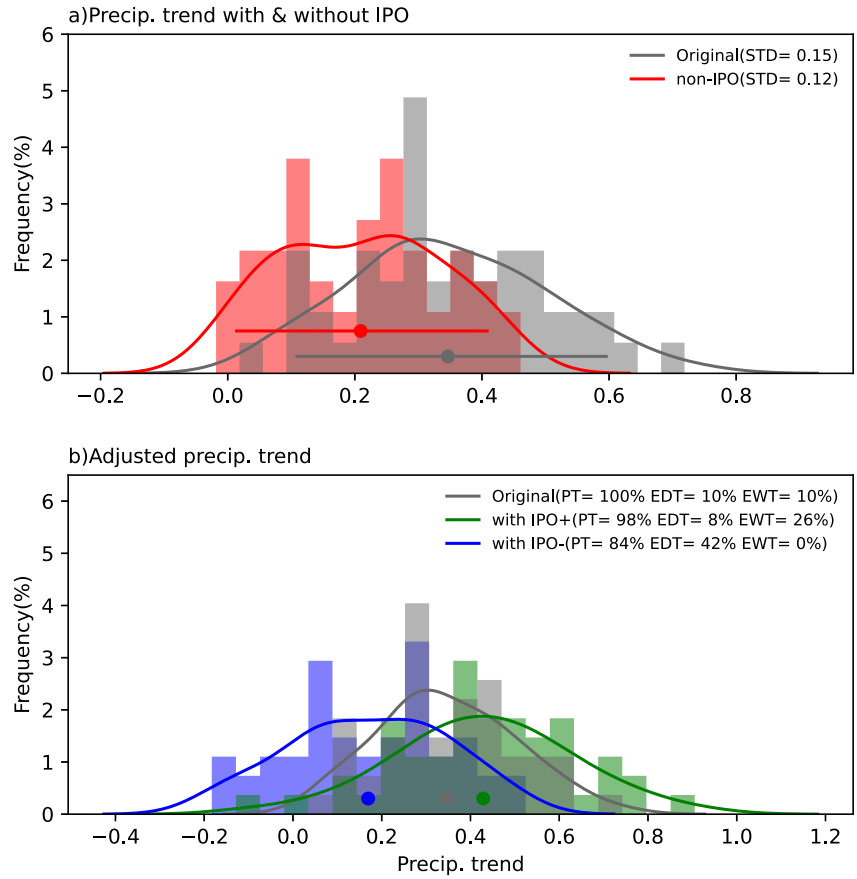

Figure 4. (a) Histograms (bars) and fitted distribution (lines) of winter northern European precipitation (WNEP) trends (units: mm day^{-1} (35-year)$^{-1}$) for ensemble members under the SSP5–8.5 scenario in CanESM5 during 2015–2050. Dots and horizontal lines represent the ensemble mean and 5–95th percentile range, respectively. The red and gray denote the original WNEP trends with and without IPO, respectively. panel (b) Same as panel (a), but the green and blue denote the WNEP trends adjusted with the positive (+2 (35-year)$^{-1}$) and negative (−2 (35-year)$^{-1}$) phase transition of IPO, respectively.

and extending across the Atlantic (Figure 3i). Notably, a highly similar circulation pattern is reproduced in the atmospheric general circulation model ECHAM6 sensitivity experiment forced with IPO-like SST anomalies (Figure S9 in Supporting Information S1; detailed in Text S6 in Supporting Information S1). High-pressure anomalies and enhanced low-level moisture divergence over northern Europe are also associated with the negative phase of the leading November IPO, serving as a precursor signal of the ensuing drier WNEP conditions (Figure S10 in Supporting Information S1). This dominant influence of horizontal and vertical dynamical components over northern Europe helps explain the observed WNEP drying pattern (Figure 2d), and these dynamics can be observed in MIROC6 as well (Figure S11 in Supporting Information S1).

To better understand how phase shifts of IPO influence WNEP changes and to qualify the extent to which IPO phase transitions could narrow precipitation projections, we remove the IPO-dependent changes in each ensemble member and compare the probability densities of original and extracted non-IPO trends (Figure 4a). The results show that IPO phase shifts could account for 20% of precipitation variability during 2015–2050, reducing inter-member variability from 0.15 to 0.12 mm day^{-1} (35-year)$^{-1}$. A complementary sensitivity analysis using quantile regression ($q = 0.5$), which assesses the dependence of the conditional WNEP median on the IPO index, further reduces the spread to 0.11 mm day^{-1} (35-year)$^{-1}$ in CanESM5, reinforcing the robustness of the linear scaling. Meanwhile, the range between 5th and 95th percentile decreases by 20% from 0.10 to 0.60 mm day^{-1} (35-year)$^{-1}$ to 0.01–0.41 mm day^{-1} (35-year)$^{-1}$. We further set up a scenario assuming an IPO transition ($\frac{\partial \mathrm{IPO}(i,t)}{\partial t}$) with a magnitude of 2 STD in the near future. The subsequent adjustment steps follow those used for the historical period. Here, a +2 STD transition can be understood as a shift from −1 to +1 STD, representing a negative-to-positive phase change, or vice versa for a positive-to-negative shift. Such a 35-year transition is reasonable, as it

19448007, 2026, 3, Downloaded from https://agupubs.onlinelibrary.wiley.com/doi/10.1029/2025GL119484 by Gang Huang - Institution Of Atmospheric Physics , Wiley Online Library on [02/02/2026]. See the Terms and Conditions (https://onlinelibrary.wiley.com/terms-and-conditions) on Wiley Online Library for rules of use; OA articles are governed by the applicable Creative Commons License

19448007, 2026, 3, Downloaded from https://agupubs.onlinelibrary.wiley.com/doi/10.1029/2025GL119484 by Gang Huang - Institution Of Atmospheric Physics , Wiley Online Library on [02/02/2026]. See the Terms and Conditions (https://onlinelibrary.wiley.com/terms-and-conditions) on Wiley Online Library for rules of use; OA articles are governed by the applicable Creative Commons License

has been observed historically (Dong & Dai, 2015) and is well captured in IPO simulations, with simulated transitions ranging from −4.59 to 4.52 over 35-year with an STD of ±2.83 (Figure S5a in Supporting Information S1).

The reconstructed WNEP trends ($\frac{\partial P_{adj}(i)}{\partial t}$) for the near future are estimated by adding back the above assumed IPO-driven WNEP trends, with each ensemble member preserving the same phase transition. Under a negative-to-positive IPO shift and SSP5–8.5 emission scenario, the ensemble-mean WNEP changes are 0.21 mm day^{-1} (35-year)$^{-1}$, drier than the original 0.34 mm day^{-1} (35-year)$^{-1}$. While the original probabilities of EDT and EWT are both 10%, an assumed positive-to-negative IPO shift increases the EDT probability to 42% while eliminates EWT. In contrast, an assumed negative-to-positive IPO transition raises the ensemble mean trend to 0.43 mm day^{-1} (35-year)$^{-1}$, reduces EDT to 8%, and increases EWT to 26% (Figure 4b). These results underscore the important modulation of IPO phase transition on WNEP changes, especially in shaping the frequency of hydroclimatic extremes. Specifically, a shift toward a negative IPO phase tends to favor droughts, whereas a positive IPO phase is associated with increased flooding. Additionally, the uncertainty in these projections becomes more challenging to constrain due to the wider inter-member spread in MIROC6. Although the spread narrows by 29% from 0.17 to 0.12 mm day^{-1} (35-year)$^{-1}$ in both linear and quantile regressions, the 5th to 95th percentile range only slightly shifts from −0.23–0.28 mm day^{-1} (35-year)$^{-1}$ to −0.24–0.20 mm day^{-1} (35-year)$^{-1}$, indicating modest improvement compared to CanESM5 (Figure S12 in Supporting Information S1). Meanwhile, similar patterns with slight amplitude differences are found in MIROC6, reinforcing the findings that IPO phase transitions significantly modulate WNEP trends and associated extremes.

4. Conclusion and Discussions

Persistent WNEP deficits are accompanied by La Niña-like SST anomalies at interannual timescales and negative IPO-like anomalies at interdecadal timescales. Based on large ensemble simulations from CanESM5 and MIROC6, internal variability, particularly the IPO, accounts for a large fraction of WNEP variability. The observed positive-to-negative shift of IPO phase contributes to drier conditions in northern Europe. After constraining inter-member spread, model simulations better align with observations, indicating a generally drier contribution of −0.07 mm day^{-1} (35-year)$^{-1}$ associated with observed negative IPO trend scenario—offsetting much of the anthropogenic wetting trend of 0.19 mm day^{-1} (35-year)$^{-1}$. Notably, the uncertainty in simulated WNEP trends decreases from 0.15 to 0.13 mm day^{-1} (35-year)$^{-1}$. Given the persistent strong correlation between IPO and WNEP, the IPO is also projected to explain 20% inter-member spread of WNEP changes in the near future. Mechanistically, this influence is primarily exerted through modulation of dynamical moisture transport with anomalous horizontal divergence and subsidence. The transition from a positive to negative IPO phase induces a significant geopotential height anomaly over northern Europe, characterized by an anticyclonic circulation that suppresses precipitation. It is worth noting that uncertainty constraint on near-future WNEP trends in the present study relies on a sensitivity framework of fixed IPO trends as ±2 STD, rather than deterministic projections, due to limitations of capturing IPO phase-evolution in Coupled Model Intercomparison Project models (Du & Chen, 2024; Qin et al., 2024).

In addition to IPO, a weak IOD-like SST anomaly over the Indian Ocean (Figure 3g), significantly correlated with IPO index, may amplify the IPO's effects. Regression analyses show that the IOD-like SST anomalies can reinforce IPO-induced circulation patterns, particularly in early winter (December–January), intensifying the drying trend in WNEP (Figure S13 in Supporting Information S1). This constructive interference weakens by February, consistent with previous findings in the historical period (Abid et al., 2021). Moreover, the contributions of interannual climate modes such as Niño 3.4 (Rayner et al., 2003) and NAO (Schneider et al., 2013) are also examined. For 1951–2014, the partial regression using observed IPO and AMV indicates that these two modes contribute comparably to the internal component of WNEP, with a fitting goodness (R^2) of 0.50. In contrast, adding Niño 3.4 and NAO indices does not substantially improve the explainability, yielding an R^2 of 0.56, suggesting that their limited ability to constrain WNEP. Importantly, although AMV exhibits a crucial influence on internal WNEP variability in observations, AMV does not exhibit a significant relationship with WNEP trends among the ensemble members (Figure S14 in Supporting Information S1), likely due to the complex non-linear dynamical processes at play (Mathieu et al., 2004; Tang & Li, 2024).

The present uncertainty-reduction framework, consistent with previous studies (Huang, Zhou, Dai, et al., 2020; Wu et al., 2021), constrains the areal mean WNEP trend rather than its spatial pattern. To assess whether the

19448007, 2026, 3, Downloaded from https://agupubs.onlinelibrary.wiley.com/doi/10.1029/2025GL119484 by Gang Huang - Institution Of Atmospheric Physics , Wiley Online Library on [02/02/2026]. See the Terms and Conditions (https://onlinelibrary.wiley.com/terms-and-conditions) on Wiley Online Library for rules of use; OA articles are governed by the applicable Creative Commons License

approach can be extended spatially, we conduct an empirical orthogonal function analysis. In CanESM5, EOF1 accounts for 97.5% of the total WNEP MME variance and exhibits a homogenous wetting pattern (Figure S15a in Supporting Information S1), suggesting the focus on constraining PC1. Although the PC1s projected into MME's EOF1 show a significant correlation with IPO among members ($r = 0.56$), IPO explains only 6.7% of WNEP variance (Figures S15b and S15c in Supporting Information S1), which is insufficient to yield a robust IPO-constrained reconstruction of the WNEP spatial pattern. This limitation likely stems from the substantial inter-member spread that the variance of individual-member WNEP fields captured by the MME EOF1 drops to an average of 23.7% across members (range: 3.4%–45.7%). Such degradation in explained variance prevents a stable and spatially coherent constraint from being established. Moreover, CanESM5 and MIROC6 are applied in this study as representatives of higher and lower Equilibrium Climate Sensitivity models, respectively, both providing 50-member ensembles (Scafetta, 2021; Zelinka et al., 2020). Precipitation, owing to its intrinsically weak forced response and pronounced inter-member spread, requires large ensemble sizes to achieve a sufficient SNR for robust estimation of the forced component. However, most existing large ensembles provide fewer available members, restricting multi-model assessment. Future work incorporating broader large-ensemble availability would be essential for establishing a spatially resolved constraint framework.

Conflict of Interest

The authors declare no conflicts of interest relevant to this study.

Data Availability Statement

The present study's conclusions are supported by publicly available data. The observational precipitation data sets are accessed from https://crudata.uea.ac.uk/cru/data/hrg/cru_ts_4.07/cruts.2304141047.v4.07/pre/ (Harris et al., 2020), https://opendata.dwd.de/climate_environment/GPCC/ (Schneider et al., 2022) and https://psl.noaa.gov/data/gridded/data.UDel_AirT_Precip.html (Matsuura & Willmott, 2015), respectively. Three observational data sets of SST are obtained from https://www1.ncdc.noaa.gov/pub/data/cmb/ersst/v5/netcdf (Huang et al., 2017), https://www.metoffice.gov.uk/hadobs/hadisst (Rayner et al., 2003) and https://psl.noaa.gov/data/gridded/data.kaplan_sst.html (Kaplan et al., 1998), respectively. In addition, large ensemble outputs are from https://aims2.llnl.gov/search/cmip6. Niño 3.4 and NAO index are downloaded from https://psl.noaa.gov/data/timeseries/month/Nino34/ and https://climatedataguide.ucar.edu/climate-data/hurrell-north-atlantic-oscillation-nao-index-station-based, respectively. The key codes for this study are archived in Zenodo and publicly available at https://doi.org/10.5281/zenodo.17719161 (Yao, 2025).

Acknowledgments
We sincerely appreciate the associate editor and three anonymous reviewers for their insightful comments, which have significantly enhanced the quality of this manuscript. This work is funded by the National Natural Science Foundation of China (42530606 and 42261144687).

References

Abid, M. A., Kucharski, F., Molteni, F., Kang, I.-S., Tompkins, A. M., & Almazroui, M. (2021). Separating the Indian and Pacific Ocean impacts on the Euro-Atlantic response to ENSO and its transition from early to late winter. *Journal of Climate*, *34*(4), 1531–1548. https://doi.org/10.1175/JCLI-D-20-0075.1

An, W., Xu, C., Marković, S. B., Sun, S., Sun, Y., Gavrilov, M. B., et al. (2023). Anthropogenic warming has exacerbated droughts in southern Europe since the 1850s. *Communications Earth & Environment*, *4*(1), 232. https://doi.org/10.1038/s43247-023-00907-1

Bordi, I., Fraedrich, K., & Sutera, A. (2009). Observed drought and wetness trends in Europe: An update. *Hydrology and Earth System Sciences*, *13*(8), 1519–1530. https://doi.org/10.5194/hess-13-1519-2009

Brönnimann, S. (2007). Impact of El Niño–Southern oscillation on European climate. *Reviews of Geophysics*, *45*(3). https://doi.org/10.1029/2006RG000199

Caloiero, T., Veltri, S., Caloiero, P., & Frustaci, F. (2018). Drought analysis in Europe and in the Mediterranean basin using the standardized precipitation index. *Water*, *10*(8), 1043. https://doi.org/10.3390/w10081043

Cammalleri, C., Naumann, G., Mentaschi, L., Formetta, G., Forzieri, G., Gosling, S., et al. (2020). *Global warming and drought impacts in the EU*. Publications Office of the European Union: Luxembourg.

Christidis, N., & Stott, P. A. (2022). Human influence on seasonal precipitation in Europe. *Journal of Climate*, *35*(15), 5215–5231. https://doi.org/10.1175/JCLI-D-21-0637.1

Deser, C., Hurrell, J. W., & Phillips, A. S. (2017). The role of the North Atlantic Oscillation in European climate projections. *Climate Dynamics*, *49*(9), 3141–3157. https://doi.org/10.1007/s00382-016-3502-z

Deser, C., Lehner, F., Rodgers, K. B., Ault, T., Delworth, T. L., DiNezio, P. N., et al. (2020). Insights from Earth system model initial-condition large ensembles and future prospects. *Nature Climate Change*, *10*(4), 277–286. https://doi.org/10.1038/s41558-020-0731-2

Dogar, M. M., Hermanson, L., Scaife, A. A., Visioni, D., Zhao, M., Hoteit, I., et al. (2023). A review of El niño Southern oscillation linkage to strong volcanic eruptions and post-volcanic Winter warming. *Earth Systems and Environment*, *7*(1), 15–42. https://doi.org/10.1007/s41748-022-00331-z

Dogar, M. M., Watanabe, S., Fujiwara, M., Abid, M. A., Habeebullah, T. M., & Khan, B. (2025). Tropical volcanic impacts on MENA climate via ENSO and NAO dynamics in a high-top model. *npj Climate and Atmospheric Science*, *8*(1), 330. https://doi.org/10.1038/s41612-025-01201-x

Dong, B., & Dai, A. (2015). The influence of the interdecadal Pacific oscillation on temperature and precipitation over the globe. *Climate Dynamics*, *45*(9), 2667–2681. https://doi.org/10.1007/s00382-015-2500-x

Du, Y., & Chen, H. (2024). Evaluation of CMIP6 model performance in simulating the PDO and its future change. *Atmospheric and Oceanic Science Letters*, *17*(3), 100449. https://doi.org/10.1016/j.aosl.2023.100449
Fereday, D., Chadwick, R., Knight, J., & Scaife, A. A. (2018). Atmospheric dynamics is the largest source of uncertainty in future winter European rainfall. *Journal of Climate*, *31*(3), 963–977. https://doi.org/10.1175/jcli-d-17-0048.1
García-Herrera, R., Garrido-Perez, J. M., Barriopedro, D., Ordóñez, C., Vicente-Serrano, S. M., Nieto, R., et al. (2019). The European 2016/17 drought. *Journal of Climate*, *32*(11), 3169–3187. https://doi.org/10.1175/JCLI-D-18-0331.1
Garrido-Perez, J. M., Vicente-Serrano, S. M., Barriopedro, D., García-Herrera, R., Trigo, R., & Beguería, S. (2024). Examining the outstanding Euro-Mediterranean drought of 2021–2022 and its historical context. *Journal of Hydrology*, *630*, 130653. https://doi.org/10.1016/j.jhydrol.2024.130653
Gouirand, I., & Moron, V. (2003). Variability of the impact of El Nino-Southern oscillation on sea-level pressure anomalies over the North Atlantic in January to March (1874-1996). *International Journal of Climatology*, *23*(13), 1549–1566. https://doi.org/10.1002/joc.963
Harris, I., Osborn, T. J., Jones, P., & Lister, D. (2020). Version 4 of the CRU TS monthly high-resolution gridded multivariate climate dataset [Dataset]. *Scientific Data*, *7*(1). https://doi.org/10.1038/s41597-020-0453-3.109.
Hawkins, E., & Sutton, R. (2011). The potential to narrow uncertainty in projections of regional precipitation change. *Climate Dynamics*, *37*(1–2), 407–418. https://doi.org/10.1007/s00382-010-0810-6
Herweijer, C., & Seager, R. (2008). The global footprint of persistent extra-tropical drought in the instrumental era. *International Journal of Climatology: A Journal of the Royal Meteorological Society*, *28*(13), 1761–1774. https://doi.org/10.1002/joc.1590
Hoerling, M., Eischeid, J., Perlwitz, J., Quan, X., Zhang, T., & Pegion, P. (2012). On the increased frequency of Mediterranean drought. *Journal of Climate*, *25*(6), 2146–2161. https://doi.org/10.1175/jcli-d-11-00296.1
Huang, B., Thorne, P. W., Banzon, V. F., Boyer, T., Chepurin, G., Lawrimore, J. H., et al. (2017). Extended reconstructed sea surface temperature, version 5 (ERSSTv5): Upgrades, validations, and intercomparisons [Dataset]. *Journal of Climate*, *30*(20), 8179–8205. https://doi.org/10.1175/JCLI-D-16-0836.1
Huang, X., Zhou, T., Dai, A., Li, H., Li, C., Chen, X., et al. (2020). South Asian summer monsoon projections constrained by the interdecadal Pacific oscillation. *Science Advances*, *6*(11), eaay6546. https://doi.org/10.1126/sciadv.aay6546
Huang, X., Zhou, T., Turner, A., Dai, A., Chen, X., Clark, R., et al. (2020). The Recent decline and recovery of Indian summer monsoon rainfall: Relative roles of external forcing and internal variability. *Journal of Climate*, *33*(12), 5035–5060. https://doi.org/10.1175/JCLI-D-19-0833.1
Ionita, M., Lohmann, G., Rimbu, N., Chelcea, S., & Dima, M. (2012). Interannual to decadal summer drought variability over Europe and its relationship to global sea surface temperature. *Climate Dynamics*, *38*(1–2), 363–377. https://doi.org/10.1007/s00382-011-1028-y
Ionita, M., & Nagavciuc, V. (2021). Changes in drought features at the European level over the last 120 years. *Natural Hazards and Earth System Sciences*, *21*(5), 1685–1701. https://doi.org/10.5194/nhess-21-1685-2021
Kaplan, A., Cane, M. A., Kushnir, Y., Clement, A. C., Blumenthal, M. B., & Rajagopalan, B. (1998). Analyses of global sea surface temperature 1856–1991 [Dataset]. *Journal of Geophysical Research*, *103*(C9), 18567–18589. https://doi.org/10.1029/97jc01736
Laaha, G., Gauster, T., Tallaksen, L. M., Vidal, J. P., Stahl, K., Prudhomme, C., et al. (2017). The European 2015 drought from a hydrological perspective. *Hydrology and Earth System Sciences*, *21*(6), 3001–3024. https://doi.org/10.5194/hess-21-3001-2017
Mathieu, P.-P., Sutton, R. T., Dong, B., & Collins, M. (2004). Predictability of Winter climate over the north Atlantic european Region during ENSO events. *Journal of Climate*, *17*(10), 1953–1974. https://doi.org/10.1175/1520-0442(2004)017<1953:POWCOT>2.0.CO;2
Matsuura, K., & Willmott, C. (2015). *Terrestrial air temperature: 1900–2008 gridded monthly time series (version 4.01)*. University of Delaware Dept. of Geography Center.
McKenna, C. M., & Maycock, A. C. (2022). The role of the north Atlantic oscillation for projections of Winter mean precipitation in Europe. *Geophysical Research Letters*, *49*(19), e2022GL099083. https://doi.org/10.1029/2022GL099083
Molteni, F., & Brookshaw, A. (2023). Early-and late-winter ENSO teleconnections to the Euro-Atlantic region in state-of-the-art seasonal forecasting systems. *Climate Dynamics*, *61*(5), 2673–2692. https://doi.org/10.1007/s00382-023-06698-7
Peña-Angulo, D., Vicente-Serrano, S. M., Domínguez-Castro, F., Murphy, C., Reig, F., Tramblay, Y., et al. (2020). Long-term precipitation in Southwestern Europe reveals no clear trend attributable to anthropogenic forcing. *Environmental Research Letters*, *15*(9), 094070. https://doi.org/10.1088/1748-9326/ab9c4f
Qin, Z., Wang, T., Chen, H., & Gao, Y. (2024). Performance of CMIP5 and CMIP6 models in reproducing the Interdecadal Pacific Oscillation and its global impacts. *International Journal of Climatology*, *44*(11), 3742–3765. https://doi.org/10.1002/joc.8548
Rakovec, O., Samaniego, L., Hari, V., Markonis, Y., Moravec, V., Thober, S., et al. (2022). The 2018–2020 multi-year drought sets a new benchmark in Europe. *Earth's Future*, *10*(3), e2021EF002394. https://doi.org/10.1029/2021EF002394
Rao, J., Ren, R., Xia, X., Shi, C., & Guo, D. (2019). Combined impact of El niño–southern oscillation and Pacific decadal oscillation on the Northern Winter stratosphere. *Atmosphere*, *10*(4), 211. https://doi.org/10.3390/atmos10040211
Rayner, N., Parker, D. E., Horton, E., Folland, C. K., Alexander, L. V., Rowell, D., et al. (2003). Global analyses of sea surface temperature, sea ice, and night marine air temperature since the late nineteenth century [Dataset]. *Journal of Geophysical Research*, *108*(D14), 4407. https://doi.org/10.1029/2002JD002670
Samset, B. H., Sand, M., Smith, C. J., Bauer, S. E., Forster, P. M., Fuglestvedt, J. S., et al. (2018). Climate impacts from a removal of anthropogenic aerosol emissions. *Geophysical Research Letters*, *45*(2), 1020–1029. https://doi.org/10.1002/2017GL076079
Scafetta, N. (2021). Testing the CMIP6 GCM Simulations versus Surface Temperature Records from 1980–1990 to 2011–2021: High ECS is not supported. *Climate*, *9*(11), 161. https://doi.org/10.3390/cli9110161
Scaife, A. A., Arribas, A., Blockley, E., Brookshaw, A., Clark, R. T., Dunstone, N., et al. (2014). Skillful long-range prediction of European and North American winters. *Geophysical Research Letters*, *41*(7), 2514–2519. https://doi.org/10.1002/2014GL059637
Schneider, D. P., Deser, C., Fasullo, J., & Trenberth, K. E. (2013). Climate data guide spurs discovery and understanding. *Eos Trans. AGU*, *94*(13), 121–122. https://doi.org/10.1002/2013EO130001
Schneider, U., Hänsel, S., Finger, P., Rustemeier, E., & Ziese, M. (2022). GPCC full data monthly product version 2022 at 0.5°: Monthly land-surface precipitation from rain-gauges built on GTS-based and historical data [Dataset]. *Global Precipitation Climatology Centre*. https://doi.org/10.5676/DWD_GPCC/FD_M_V2022_050
Shaman, J., & Tziperman, E. (2011). An atmospheric teleconnection linking ENSO and Southwestern European precipitation. *Journal of Climate*, *24*(1), 124–139. https://doi.org/10.1175/2010JCLI3590.1
Spinoni, J., Vogt, J. V., Naumann, G., Barbosa, P., & Dosio, A. (2018). Will drought events become more frequent and severe in Europe?
Swart, N. C., Cole, J. N. S., Kharin, V. V., Lazare, M., Scinocca, J. F., Gillett, N. P., et al. (2019). The Canadian Earth System Model version 5 (CanESM5.0.3) [Dataset]. *Geoscientific Model Development*, *12*(11), 4823–4873. https://doi.org/10.5194/gmd-12-4823-2019
Tang, X., & Li, J. (2024). Synergistic effect of boreal autumn SST over the tropical and South Pacific and winter NAO on winter precipitation in the southern Europe. *npj Climate and Atmospheric Science*, *7*(1), 78. https://doi.org/10.1038/s41612-024-00628-y

19448007, 2026, 3, Downloaded from https://agupubs.onlinelibrary.wiley.com/doi/10.1029/2025GL119484 by Gang Huang - Institution Of Atmospheric Physics , Wiley Online Library on [02/02/2026]. See the Terms and Conditions (https://onlinelibrary.wiley.com/terms-and-conditions) on Wiley Online Library for rules of use; OA articles are governed by the applicable Creative Commons License

Tatebe, H., Ogura, T., Nitta, T., Komuro, Y., Ogochi, K., Takemura, T., et al. (2019). Description and basic evaluation of simulated mean state, internal variability, and climate sensitivity in MIROC6. *Geoscientific Model Development*, *12*(7), 2727–2765. https://doi.org/10.5194/gmd-12-2727-2019

Toreti, A., Bavera, D., Acosta Navarro, J., Cammalleri, C., de Jager, A., Di Ciollo, C., et al. (2022). *Drought in Europe August 2022*. Publications Office of the European Union: Luxembourg.130493.

Trnka, M., Balek, J., Stepanek, P., Zahradníček, P., Mozny, M., Eitzinger, J., et al. (2016). Drought trends over part of Central Europe between 1961 and 2014. *Climate Research*, *70*. https://doi.org/10.3354/cr01420

van der Woude, A. M., Peters, W., Joetzjer, E., Lafont, S., Koren, G., Ciais, P., et al. (2023). Temperature extremes of 2022 reduced carbon uptake by forests in Europe. *Nature Communications*, *14*(1), 6218. https://doi.org/10.1038/s41467-023-41851-0

Verdon, D. C., & Franks, S. W. (2006). Long-term behaviour of ENSO: Interactions with the PDO over the past 400 years inferred from paleoclimate records. *Geophysical Research Letters*, *33*(6). https://doi.org/10.1029/2005GL025052

Vicente-Serrano, S. M., Lopez-Moreno, J.-I., Beguería, S., Lorenzo-Lacruz, J., Sanchez-Lorenzo, A., García-Ruiz, J. M., et al. (2014). Evidence of increasing drought severity caused by temperature rise in southern Europe. *Environmental Research Letters*, *9*(4), 044001. https://doi.org/10.1088/1748-9326/9/4/044001

Vicente-Serrano, S. M., Tramblay, Y., Reig, F., González-Hidalgo, J. C., Beguería, S., Brunetti, M., et al. (2025). High temporal variability not trend dominates Mediterranean precipitation. *Nature*, *639*(8055), 658–666. https://doi.org/10.1038/s41586-024-08576-6

Wu, M., Zhou, T., Li, C., Li, H., Chen, X., Wu, B., et al. (2021). A very likely weakening of Pacific Walker Circulation in constrained near-future projections. *Nature Communications*, *12*(1), 6502. https://doi.org/10.1038/s41467-021-26693-y

Yao, M. (2025). Key_codes_GRL. *Zenodo*. https://doi.org/10.5281/zenodo.17719161

Yu, B., & Zwiers, F. (2007). The impact of combined ENSO and PDO on the PNA climate: A 1,000-year climate modeling study. *Climate Dynamics*, *29*(7–8), 837–851. https://doi.org/10.1007/s00382-007-0267-4

Zelinka, M. D., Myers, T. A., McCoy, D. T., Po-Chedley, S., Caldwell, P. M., Ceppi, P., et al. (2020). Causes of higher climate sensitivity in CMIP6 models. *Geophysical Research Letters*, *47*(1), e2019GL085782. https://doi.org/10.1029/2019GL085782

References From the Supporting Information

Giorgetta, M. A., Jungclaus, J., Reick, C. H., Legutke, S., Bader, J., Böttinger, M., et al. (2013). Climate and carbon cycle changes from 1850 to 2100 in MPI-ESM simulations for the Coupled Model Intercomparison Project phase 5. *Journal of Advances in Modeling Earth Systems*, *5*(3), 572–597. https://doi.org/10.1002/jame.20038

Li, L., Li, W., & Barros, A. P. (2013). Atmospheric moisture budget and its regulation of the summer precipitation variability over the southeastern United States. *Climate Dynamics*, *41*(3–4), 613–631. https://doi.org/10.1007/s00382-013-1697-9

Lin, R., Zhou, T., & Qian, Y. (2014). Evaluation of global monsoon precipitation changes based on five reanalysis datasets. *Journal of Climate*, *27*(3), 1271–1289. https://doi.org/10.1175/JCLI-D-13-00215.1

Liu, Y., Cai, W., Zhang, Y., Lin, X., & Li, Z. (2024). Near-term projection of Amazon rainfall dominated by phase transition of the Interdecadal Pacific Oscillation. *npj Climate and Atmospheric Science*, *7*(1), 46. https://doi.org/10.1038/s41612-024-00587-4

Mantua, N. J., Hare, S. R., Zhang, Y., Wallace, J. M., & Francis, R. C. (1997). A Pacific interdecadal climate oscillation with impacts on salmon production*. *Bulletin of the American Meteorological Society*, *78*(6), 1069–1080. https://doi.org/10.1175/1520-0477(1997)078<1069:APICOW>2.0.CO;2

Seager, R., Naik, N., & Vecchi, G. A. (2010). Thermodynamic and dynamic mechanisms for large-scale changes in the hydrological cycle in response to global warming. *Journal of Climate*, *23*(17), 4651–4668. https://doi.org/10.1175/2010JCLI3655.1

Stevens, B., Giorgetta, M., Esch, M., Mauritsen, T., Crueger, T., Rast, S., et al. (2013). Atmospheric component of the MPI-M Earth system model: ECHAM6. *Journal of Advances in Modeling Earth Systems*, *5*(2), 146–172. https://doi.org/10.1002/jame.20015

Yao, M., Tang, H., & Huang, G. (2024). Inter-Model uncertainty in projecting precipitation changes over central Asia under global warming. *Geophysical Research Letters*, *51*(24), e2024GL111989. https://doi.org/10.1029/2024GL111989

19448007, 2026, 3, Downloaded from https://agupubs.onlinelibrary.wiley.com/doi/10.1029/2025GL119484 by Gang Huang - Institution Of Atmospheric Physics , Wiley Online Library on [02/02/2026]. See the Terms and Conditions (https://onlinelibrary.wiley.com/terms-and-conditions) on Wiley Online Library for rules of use; OA articles are governed by the applicable Creative Commons License